Atom Indonesia Vol. 36 No. 3 (2010) 95 - 104

Modelling of Ion Transport in Solids with a General Bond Valence Based Force-Field

S. Adams* **and R.P. Rao**
Department of Materials Science and Engineering,
National University of Singapore, Singapore 117574, Singapore

ARTICLE INFO

Article history:
Received 11 October 2010
Received in revised form 26 October 2010
Accepted 28 October 2010

Keywords:
Bond valence
Electrode
Lithium ion battery
Lithium ion pathways
Molecular dynamic method
Solid electrolyte

ABSTRACT

Empirical bond length - bond valence relations provide insight into the link between structure of and ion transport in solid electrolytes. Building on our earlier systematic adjustment of bond valence (BV) parameters to the bond softness, here we discuss how the squared BV mismatch can be linked to the absolute energy scale and used as a general Morse-type interaction potential for analyzing low-energy pathways in ion conducting solid or mixed conductors either by an energy landscape approach or by molecular dynamics (MD) simulations. For a wide range of Lithium oxides we could thus model ion transport revealing significant differences to an earlier geometric approach. Our novel BV-based force-field has also been applied to investigate a range of mixed conductors, focusing on cathode materials for lithium ion battery (LIB) applications to promote a systematic design of LIB cathodes that combine high energy density with high power density. To demonstrate the versatility of the new BV-based force-field it is applied in exploring various strategies to enhance the power performance of safe low cost LIB materials ($LiFePO_4$, $LiVPO_4F$, $LiFeSO_4F$, etc.).

INTRODUCTION

Understanding ionic motion in disordered solids obviously requires insight into the correlation between ion mobility and the structural and energetic local environment of the mobile ions. Local structure models for disordered solid electrolytes such as ion conducting glasses may in principle be derived from diffraction data (crystal structure refinements for crystalline phases or reverse Monte Carlo (RMC) fitting for glassy phases) or molecular dynamics (MD) simulations [1,2]. In principle, MD simulations permit to derive comprehensive structural and dynamical information within the limitations imposed by the system size, the simulated period and the agreement of the employed interaction potential parameters with reality. Effectively both approaches have shown to be valuable tools in obtaining insights into the conduction mechanism and its correlation to the atomic structure, though in the case of MD simulations it has to be verified that the force field chosen for the simulations leads to structure models that are consistent with experimental information [2-4].

* Corresponding author.
E-mail address: mseasn@nus.edu.sg (S. Adams)

In this work, we discuss how the bond valence (BV) method can be used to predict characteristics of ionic conductivity from structure models [4-7], and be optimized by linking it to an absolute energy scale for a more straightforward comparison with other atomistic simulation and modelling approaches.

EXPERIMENTAL METHODS

Empirical relationships between bond length R and bond valence $s_{A\text{-}X} = \exp[(R_0-R)/b]$ are widely used in crystal chemistry to identify plausible equilibrium sites for an atom in a structure as sites where the BV sum of the atom matches its oxidation state (see *e.g.* the recent review by Brown [5] and references therein). In our earlier work, we introduced a systematic adjustment of BV parameters to the bond softness [6-9], which together with the inclusion of interactions beyond the first coordination shell permits more adequate estimates of non-equilibrium site energies. The inclusion of weak interactions to more distant counterions beyond the first coordination shell is indispensable for modelling ion transport pathways as it avoids artefacts in the BV variation, when an ion moves across the border of its coordination shell. Low BV sum mismatch (and hence low

energy) pathways for a cation A^+ can then be modelled as regions in the structure, where the bond valence sum $V(A)= \Sigma s_{A-X}$ (summing up over all adjacent counterions X) approaches the ideal valence $V_{id}(A)$ (i.e. its oxidation state).

To enhance chemical plausibility "BV mismatch landscapes" $|\Delta V(A)|$ various additional penalty functions p_{A-X} have been introduced that (i) discriminate against sites, where a matching V(A) is achieved by strongly asymmetric coordinations (details are described in [3, 6]) and (ii) exclude sites close to other (immobile) cation types. The cation-cation penalty functions may simply take the form of exclusion radii, but truncated Coulomb repulsions yield a more physical description. Interactions among mobile cations are intentionally left out at this stage. While it is obvious that a higher BV mismatch implies an energetically less favourable state, a direct link of the type

$$E = D_0 \cdot |\Delta V|^g + E_{asym} + E_{rep} = D_0 \cdot \left| \sum_X s_{A-X} - V_{id}(A) \right|^g + E_{asym} + E_{rep} \quad (1)$$

remained to be established [4]. In eq. (1), E_{asym} represents an energy penalty term due to the asymmetry of the coordination of the considered ion and E_{rep} the (Coulomb) repulsion between mobile and immobile cations.

RESULTS AND DISCUSSION

Bond valence based force field

An empirical approach to assess the coefficients D_0 and g of eq. (1) as well as a suitable functional form for E_{asym} may start from comparing the interaction distance dependence of the BV sum mismatch with the distance dependence of interaction energy in empirical interatomic potentials. The variation of an individual bond valence can be integrated in a Morse-type potential

$$E = D_0 \left\{ (\exp[\alpha(R_{\min} - R)] - 1)^2 - 1 \right\} = D_0 \left\{ \left(\frac{\exp\left[\frac{R_0 - R}{b}\right] - s_{\min}}{s_{\min}} \right)^2 - 1 \right\} \quad (2)$$

with the BV parameter $b = 1/\alpha$, implying that the interaction energy E can be approximated as a quadratic function of the deviation of the BVsum from its value $s_{min} = \exp[(R_0-R_{\min})/b]$ for the energy minimum distance ($R = R_{\min}$) and hence the parameter g in equation (1) is simply 2. Note that the BV parameter R_0 (the distance corresponding to $s = 1$) generally differs from R_{min} in (the bond distance for which the interaction potential yields an energy minimum). By introducing the relative bond valence $s_{rel} = s/s_{min}$ the Morse potential of eq. 2 can be expressed in a compact notation [4]:

$$E = D_0 \left\{ \frac{(s - s_{\min})^2}{s_{\min}^2} - 1 \right\} = D_0 \left(s_{rel}^2 - 2 s_{rel} \right) \quad (3)$$

The Morse-type interaction potential expressed in eq. (2) is characterised by the three parameters D_0 , $R_{\min}$ and α that have to be linked to the BV parameters. As mentioned above, α can simply be identified with $1/b$. A tentative approach to establish a consistent set of R_{min} (or s_{min}) values may be expressed as

$$R_{\min} \approx R_0 \times \left[0.9185 + 0.2285 \cdot |\sigma_A - \sigma_X| \right] - b \cdot \ln\left(\frac{V_{id}}{CN} \right) \quad (4)$$

where CN refers to the preferred coordination number of the central ion (for examples see Table 1) and the empirically determined term in square brackets accounts for the effect of polarisation (σ_A, σ_X refer to the absolute softnesses of the cation and anion, respectively; see *e.g.*, ref. [8]) as well as the influence of higher coordination shells.

For the Morse-type interaction potential expressed in eq. (2) or (3) the dissociation energy D_0 can be expected to be $D_0 = b^2\, k/2$, k being the force constant at the distance $R = R_{min}$. We have thus approximated D_0 for a wide range of cations as

$$D_0 = \frac{k \cdot b^2}{2} = c \cdot 14.4 \frac{eV}{\text{Å}} \cdot \frac{\frac{(V_{id}(A) \cdot V_{id}(X))^{1/c}}{\sqrt{n_A \cdot n_X}}}{R_{\min}} \times \frac{b^2}{2} \quad (5)$$

with $c = 1$ if A is an *s* or *p* block elements, $c = 2$ if s is a *d* or *f* block elements. n_A, n_X represent the principal quantum numbers of cation A and anion X and $V_{id}(A)$, $V_{id}(X)$ their respective nominal charges.

In contrast to the conventional BV sum mismatch description, such BV interaction potentials of the type described in eqs. (2) or (3) fulfil the formal requirements for an anharmonic diatomic interaction potential, allowing for a molecular dynamics simulation based on BV parameters. Due to the ready availability of BV parameters for a wide range of cation anion pairs this might be an attractive option. In table 1 we list as an example parameters derived by the above formalism from our respective softBV bond valence parameters [8, 9] for the interaction of 147 cation types with O^{2-} in compounds that do not contain other types of anions. With these definitions of the energy of a single bond, the total site energy *E(A)* of a cation A, can then be determined as the sum over BV terms for the interactions with each of the N adjacent anions X_i :

$$E_{pot}(A) = D_0 \left[\sum_{j=1}^{N} \left(\frac{s_{A-Xj} - s_{\min}}{s_{\min}} \right)^2 - N \right] \quad (6)$$

By rewriting eq.(6) it becomes obvious that the total potential energy varies with both the mismatch of the bond valence sum and the asymmetry of the coordination. This allows to quantify the correlation between

1. the *bond valence sum rule* [10], stating that that the sum of the bond valences around an atom is equal to its atomic valence; and
2. and the *equal valence rule* [10], which states that the sum of the bond valences around any loop is zero, is that the most symmetric distribution of atomic valence among the bonds is energetically preferable.

If for the sake of simplicity only contributions from the N_C counterions of type X in the first coordination shell around the cation A are considered in the derivation, the correlation takes the simple form of eq. (7):

$$E_{pot}(A) = D_0\left[N_C \cdot \left\{ \left(\frac{V(A) - V_{\min}(A)}{V_{\min}(A)} \right)^2 - 1 \right\} + \sum_{i=1}^{N_C} \left(\frac{s_{A-X} - \bar{s}_{A-X}}{s_{\min}} \right)^2 \right] \quad (7)$$

where $V_{min}(A) = N_C \times s_{min}$ in the first term (the BV sum mismatch term), while the second term (the asymmetry term) quantifies the effect of the deviation of individual bond valences from their average value $\bar{s}_{A\text{-}X} = V(A)/N_C$ [4].

A major advantage of such an energy-scaled BV mismatch is that it allows straightforward combinations of the BV sum term as an effective "attraction term" with suitably weighted penalty functions for coordination asymmetry and particularly a Coulombic cation-cation repulsion. To model Coulomb repulsion we will throughout this paper use fractional charges q_A, q_X that are calculated based on the formulas

$$q_{Ai} = \frac{V_{id}(A_i)}{\sqrt{n_{Ai}}} \sqrt{\frac{\sum_j \frac{V_{id}(X_j)\cdot N_{Xj}}{\sqrt{n_{Xj}}}}{\sum_i \frac{V_{id}(A_i)\cdot N_{Ai}}{\sqrt{n_{Ai}}}}}, \qquad q_{Xj} = \frac{V_{id}(X_j)}{\sqrt{n_{Xj}}} \sqrt{\frac{\sum_i \frac{V_{id}(A_i)\cdot N_{Ai}}{\sqrt{n_{Ai}}}}{\sum_j \frac{V_{id}(X_j)\cdot N_{Xj}}{\sqrt{n_{Xj}}}}} \quad (8)$$

in which N_{Ai}, N_{Xj} refer to the occupancies of the i-th cation A_i or the j-th anion X_j in the structure model (typically 1). This scaling of fractional charges ensures that the model is overall charge-neutral. Obviously, fractional charges from quantum mechanical calculations could be used instead and may improve the quality of the fit, but at the expense of suitability of the approach for the fast and automatic generation of force-fields for screening of a wide range of compounds. The Coulomb repulsions e.g. between immobile A_1 and mobile A_2 cations are then taken into account in a screened version $E_{Coulomb}(A_1\text{-}A_2)$:

$$E_{Coulomb}\ (A_1 - A_2) = \frac{q_{A1} \cdot q_{A2}}{R_{A1-A2}} \cdot erfc\left(\frac{R_{A1-A2}}{\rho_{A1-A2}} \right) \quad (9)$$

The screening factor $\boldsymbol{\rho_{A1\text{-}A2} = (r_{A1} + r_{A2})\, f}$ therein is assumed to equal the sum of the covalent radii $\boldsymbol{r_{Ai}}$ of the two ions involved times a factor $\boldsymbol{f}$ that depends on the average absolute cation electronegativity and the average cation charge in the compound. Typical values of $\boldsymbol{f}$ in ternary and quaternary lithium oxides fall into the range 0.74 ± 0.04 and thereby typical values of $\boldsymbol{\rho}$ are of the order of 2 Å. While this simplification restricts long range interactions to the real part of the Ewald sum, this localized interaction model has been shown to lead to realistic activation energies of diffusion e.g. for a range of Li conducting oxyacid salts [11-13]. Due to the favourable convergence of the chosen interaction model a relatively short cut-off radius (8-10 Å) could be generally used enhancing computational efficiency.

Bond valence Lithium migration maps

Regions in the structure model, where *E(Li)* assumes low values, are - as mentioned above - assumed to belong to (BV models of) pathways for Li^+ ion migration. It is assumed that dc conduction requires continuous pathways across the unit cell in at least one dimension. These pathways are visualized as regions enclosed by isosurfaces of constant *E(Li)* based on calculations of *E(Li)* for a grid of hypothetical Li positions covering the entire unit cell with a resolution of ca 0.1 Å. The threshold value for which isosurfaces of *E(Li)* form a continuous migration pathway (that includes both occupied and vacant Li sites), permits a rough estimate of the activation energy for the Li^+ ion migration. As such an approach neglects relaxation, the assessment of the activation energy is based on an empirical correlation observed for a wide range of Lithium ion conductors. The analysis reveals significant differences to results from a recent geometric Voronoi–Dirichlet partition based study of cages and channels in crystalline Lithium oxides by Anurova *et al*. [15], which are particularly pronounced for the 33 types of ternary oxides listed in [15] as containing 1D Li pathways: In our BV based models 1D migration channels with low to moderate activation energies are observed for 19 of these structures only, while 3 exhibit 2D pathways (LT-$LiPO_3$, $Li_2W_2O_7$, Li_2TeO_3), 6 of them even 3D pathways (α-Li_3BO_3, Li_4GeO_4, Li_2SeO_4, $Li_2T_2O_5$ (T=Si, Ge), Li_4TeO_5, $Li_4Mo_5O_{17}$) and the structure models employed in [15] are questionable or implausible or do not yield any paths in further six cases. One of the main reasons for these deviations is the complex curved nature of the higher-dimensional paths, which are difficult to

identify based on a geometric approach that emphasises straight channels. Unsurprisingly the agreement is much better for the structure types suggested to be 2D- or 3D conductors in ref. [15]. The main difference is however that the pathway analysis yields energy thresholds along the pathways and hence allows a direct assessing of activation energies (Fig. 1).

Table 1. Average cation coordination numbers N_c in oxides, parameters for bond valence calculations (R_0, cut-off distance R_{co}) and the resulting Morse potential parameters D_0, R_{min}, α as determined from a wide range of stable oxide compounds. The BV parameter b is not listed here as it is identical to $1/\alpha$.

cation	N_c	R_0 / Å	R_{co} / Å	D_0 / eV	R_{min} / Å	$\alpha=1/b$ / Å^{-1}
H(1)	1.923	0.87045	4	1.8858	1.12768	2.188184
LI(1)	5.021	1.17096	5.5	0.98816	1.94001	1.937984
BE(2)	4	1.20903	5.5	2.76882	1.52217	1.848429
B(3)	3.417	1.35761	4.5	2.38924	1.34003	2.597403
C(4)	3	1.39826	5	4.79187	1.20089	2.237136
C(2)	1	1.41368	5	2.40553	1.03098	2.409639
N(5)	3	1.46267	5	6.27677	1.16142	2.222222
N(3)	2	1.40795	5	3.81089	1.13758	2.232143
NH4(1)	3.467	2.0338	6	0.40537	2.45364	2.262443
NA(1)	6.52	1.56225	6	0.57523	2.37433	2.074689
MG(2)	5.897	1.48398	5.5	1.57554	1.95627	1.953125
AL(3)	5.327	1.59901	5	1.80346	1.75806	2.358491
SI(4)	4.1	1.60817	5	2.8572	1.53594	2.314815
P(5)	4	1.62038	5	3.89635	1.44066	2.28833
P(3)	3	1.51555	4.5	2.02062	1.41051	2.487562
S(6)	4	1.6422	5	4.96726	1.38102	2.267574
S(4)	3	1.64282	5.5	3.03672	1.41188	2.34192
CL(7)	4	1.67946	5	5.991	1.34801	2.257336
CL(5)	3	1.69552	5.5	4.29089	1.35653	2.247191
CL(3)	2	1.72265	5.5	3.07119	1.38441	2.03666
K(1)	8.846	1.94117	6	0.34985	2.76636	2.293578
CA(2)	7.544	1.79519	5.5	0.99429	2.32032	2.10084
SC(3)	6.255	1.7322	5.5	2.1561	1.99615	2.024291
TI(4)	6	1.72394	5.5	2.81333	1.83144	1.988072
TI(3)	6	1.69766	5.5	1.97851	1.88619	2.173913
V(5)	4.166	1.79445	5.5	3.69533	1.60258	1.960784
V(4)	5.738	1.74932	5	2.08047	1.77638	2.347418
V(3)	6	1.67799	5.5	1.82936	1.85797	2.277904
V(2)	6	1.59976	5.5	1.64024	1.99753	2.096436
CR(6)	4	1.82471	5.5	3.68751	1.53251	2.10084
CR(5)	4	1.76781	5.5	2.36551	1.55546	2.487562
CR(4)	5.429	1.76095	5.5	1.93329	1.76209	2.444988
CR(3)	6	1.66198	5.5	1.77335	1.83887	2.325581
CR(2)	5.6	1.59356	5.5	1.69161	1.9613	2.083333
MN(7)	4	1.87362	6.5	4.9163	1.48171	1.923077
MN(6)	4	1.82018	5.5	2.82236	1.52931	2.403846
MN(5)	4	1.78879	5.5	2.46456	1.57577	2.421308
MN(4)	5.923	1.73272	5	1.85886	1.77045	2.487562
MN(3)	5.862	1.68993	5.5	1.81283	1.85786	2.28833
MN(2)	5.91	1.62758	5.5	1.64143	2.02969	2.079002
FE(3)	5.733	1.7084	5	1.66681	1.86647	2.380952
FE(2)	5.743	1.57911	5.5	1.69269	1.96005	2.083333
FE(4)	6	1.76559	5.5	1.87285	1.82786	2.439024
NI(2)	5.933	1.5592	5.5	1.46841	1.92452	2.257336
NI(4)	6	1.72159	5	1.86451	1.76508	2.487562
NI(3)	6	1.64888	5.5	1.66191	1.81887	2.415459
CO(4)	4	1.79444	5.5	2.35804	1.67959	2.267574
CO(3)	6	1.59234	5.5	1.87024	1.7762	2.304147
CO(2)	5.506	1.59773	5.5	1.51476	1.93362	2.217295
CO(1)	2	1.29501	5.5	2.39348	1.64059	1.610306
CU(3)	4	1.70964	5	1.88242	1.70823	2.34192
CU(2)	2.56	1.57422	5	1.85341	1.56633	2.227171
CU(1)	2.56	1.5873	5	0.66417	1.78269	2.932551
ZN(2)	4.718	1.65344	5	1.24031	1.88557	2.48139
GA(3)	4.905	1.71606	5	1.18456	1.79391	2.680965
GE(4)	4.305	1.73939	5	1.91375	1.66872	2.525253
AS(5)	4.029	1.76689	5	2.71934	1.58127	2.43309
AS(3)	3	1.76706	5	1.51493	1.64554	2.475248
SE(6)	4	1.79866	5.5	3.44865	1.53287	2.403846
SE(4)	3	1.80095	5.5	2.38082	1.55957	2.34192
BR(7)	4	1.83658	5.5	4.24339	1.50274	2.364066
RB(1)	10.02	2.08597	6.5	0.26813	2.89683	2.421308
SR(2)	9.4	1.95311	5.5	0.74351	2.53589	2.197802
Y(3)	7.285	1.90384	5.5	1.62701	2.21523	2.09205
ZR(4)	6.765	1.84505	5.5	2.19103	1.99602	2.040816
NB(5)	6.044	1.86588	5.5	2.72326	1.85459	2.008032
NB(4)	6	1.78543	6	2.7096	1.85989	1.901141
NB(3)	6	1.74581	6	2.02848	1.9519	1.996008
MO(6)	4.764	1.90934	5	1.9915	1.71254	2.557545
MO(5)	5.98	1.8476	5.5	2.64802	1.7867	2.074689
MO(4)	6	1.7239	6.5	3.10807	1.85099	1.779359
MO(3)	5.7	1.78933	5.5	1.42826	1.92974	2.392344
MO(2)	5.5	2.07169	5.5	0.79706	2.3496	2.369668
TC(7)	4	1.97036	6	4.04144	1.57518	1.945525
RU(6)	4.5	1.92579	5.5	2.42109	1.66431	2.352941
RU(5)	6	1.87442	5.5	2.13208	1.81571	2.293578
RU(4)	6	1.79363	5.5	1.99513	1.84053	2.227171
RU(3)	6	1.72066	5.5	1.54061	1.8932	2.325581
RH(4)	6	1.77675	5.5	1.62725	1.81793	2.48139
RH(3)	6	1.67013	5.5	1.92826	1.86915	2.09205
PD(2)	4	1.62359	5.5	1.7391	1.83671	2.008032
PD(4)	5.333	1.805	5.5	2.04218	1.79813	2.227171
AG(1)	4.438	1.78239	5	0.63519	2.22578	2.538071
AG(3)	6.25	1.84687	5.5	1.52826	2.0348	2.252252
AG(2)	5	1.72209	5.5	1.5834	2.04171	1.996008
CD(2)	6.176	1.83926	5.5	0.98346	2.1694	2.457002
TA(4)	5.5	1.75632	6	2.75655	1.79826	1.831502
IN(3)	6.024	1.90305	5	0.84076	2.02471	2.832861
SN(2)	3.325	1.87499	5.5	0.97261	1.9642	2.183406
SN(4)	6.069	1.89019	5	1.35268	1.93422	2.638522
SB(5)	6	1.89768	5.5	1.95523	1.86318	2.5
SB(3)	6	1.92036	5	1.17786	2.07526	2.364066
I(7)	5.8	1.92274	5.5	3.21424	1.74105	2.386635
I(5)	3.1	1.97775	6	2.48947	1.64421	2.358491
TE(6)	6	1.91343	5.5	2.56406	1.80876	2.427184
TE(4)	3.396	1.9529	5.5	1.67169	1.75208	2.493766
TE(2)	2	1.39168	6.5	2.62609	1.29893	1.633987
CS(1)	11.79	2.25899	6.5	0.23307	3.13121	2.386635
BA(2)	10.32	2.15998	6	0.57994	2.73769	2.28833
LA(3)	9.83	2.06392	5.5	1.18587	2.46989	2.217295
LA(3)	9.83	2.06392	5.5	1.18587	2.46989	2.217295
CE(4)	7.867	2.02821	5.5	1.48412	2.19872	2.257336
CE(3)	9.147	2.03118	5.5	1.22048	2.37861	2.227171
PR(3)	9.067	2.03652	5.5	1.17041	2.37113	2.277904
ND(3)	8.647	2.02425	5.5	1.13205	2.33016	2.336449
SM(3)	8.119	2.01168	5.5	1.17622	2.29536	2.309469
EU(3)	7.743	2.00469	5.5	1.19545	2.26888	2.304147
EU(2)	10.111	1.89158	6	1.13032	2.53846	2.024291
GD(3)	8.052	1.99654	5.5	1.09161	2.2719	2.409639
TB(4)	6	1.96244	6	1.70132	2.38506	2.024291
TB(3)	7.958	1.95675	5.5	1.20764	2.23563	2.309469
DY(3)	7.828	1.96029	5.5	1.1735	2.22689	2.347418
HO(3)	7.5	1.97099	5.5	1.12157	2.21122	2.409639
ER(3)	7.135	1.95608	5.5	1.12394	2.17477	2.427184
TM(3)	6.912	1.94901	5.5	1.18138	2.16042	2.375297
YB(3)	6.875	1.92872	5.5	1.21989	2.1422	2.347418
YB(2)	8	1.63254	5.5	1.38414	2.20942	1.960784
LU(3)	6.83	1.91728	5.5	1.19488	2.136	2.375297
HF(4)	7.105	1.83361	6	1.89992	1.99964	2.09205
TA(5)	6.09	1.86816	5.5	2.36669	1.85532	2.057613
W(6)	5.688	1.90641	5	1.84267	1.77713	2.493766
W(5)	6	1.81975	6	2.6157	1.76261	2.008032
W(4)	6	1.74558	6	2.47114	1.81945	1.923077
RE(7)	4.098	1.97792	6	3.55593	1.59634	1.968504
RE(6)	5.5	1.91007	6	2.95099	1.71147	2.008032
RE(5)	6	1.82664	6	2.41099	1.76914	2.087683
RE(4)	6	1.78237	6	2.31664	1.84497	1.972387
RE(3)	6	2.2071	6	0.81067	2.33218	2.493766
OS(8)	5.333	1.97728	6	3.71019	1.66146	1.953125
OS(7)	6	1.95775	5.5	2.91948	1.72869	2.087683
OS(6)	6	1.93192	5.5	2.44871	1.7828	2.159827
OS(4)	6	1.75302	6	2.27524	1.81244	2.008032
IR(5)	6	1.89791	6	2.32476	1.83476	2.087683
IR(4)	6	1.83233	5.5	1.68667	1.87402	2.293578
PT(4)	6	1.82198	5.5	2.03825	1.87174	2.087683
PT(3)	5	1.66559	5.5	2.35953	1.81938	1.831502
PT(2)	4	1.51205	5.5	2.14999	1.80179	1.74216
AU(3)	4	1.81761	5.5	1.96967	1.81312	2.008032
AU(1)	2	1.71819	5.5	0.85304	1.89543	2.267574
HG(2)	6.966	1.81276	5.5	1.12852	2.25275	2.150538
HG(1)	4.786	1.8128	5.5	0.73931	2.43155	2.150538
TL(3)	5.22	2.06297	5	0.67637	2.10642	2.95858
TL(1)	8.03	1.91752	6	0.34999	2.77086	2.070393
PB(4)	5.74	2.03293	5	1.02719	2.02857	2.824859
PB(2)	7.541	2.01825	5.5	0.63833	2.44191	2.309469
BI(5)	6	2.04498	5	1.4405	1.98599	2.695418
BI(3)	6.058	2.03677	5.5	0.97904	2.18321	2.415459

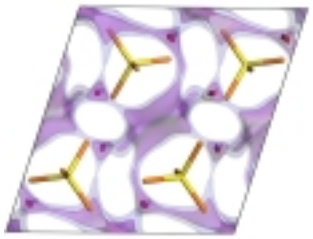

Li_2SO_4 ($P2_1/a$, 000058)

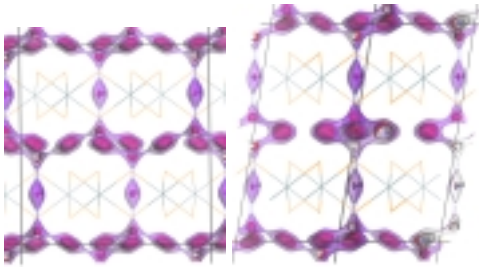

$Li_{1.8}SnO_3$ (C2/c, 035235)

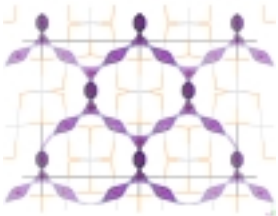

$LiTi_2O_4$ (Fd-3m, 015789).

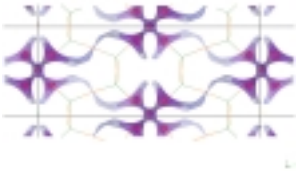

Li_2Ge_2O5 (Cc , 028178)

Li_2MnO_2 (P-3m1, 037327)

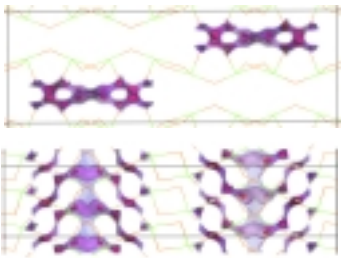

$Li_2Te_2O_5$ (Pnaa, 026452)

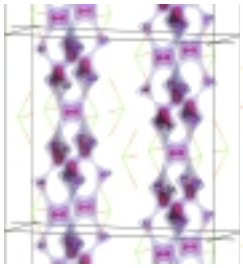

Li_2TeO_4 (C2/c, 004317)

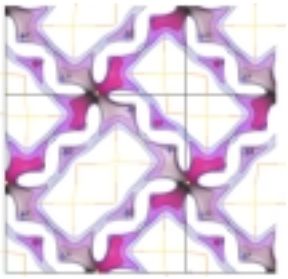

Li_3AuO_3 (P 42/mnm,015113)

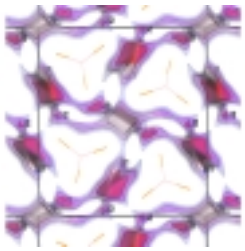

Li_3BO_3 (P2/c,009105)

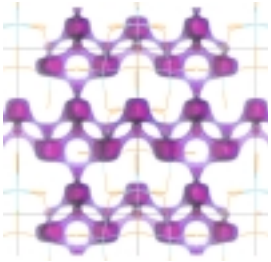

Li_3NbO_4 (I23,030246)

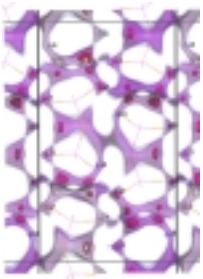

$Li_4P_2O_7$ ($P2_1/n$,039814)

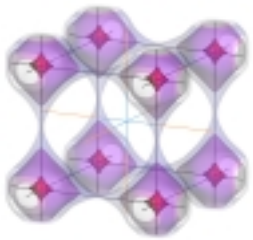

$Li_{0.93}WO_3$ (Pm-3m,028882)

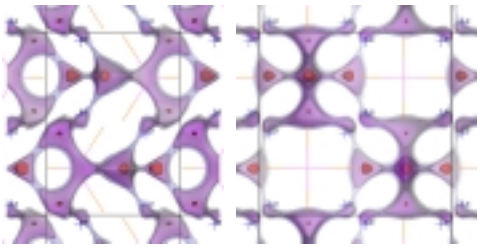

α-Li_5AlO_4 (Pbca,042697)

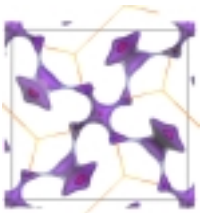

$Li_6Si_2O_7$ ($P-42_1m$,025752)

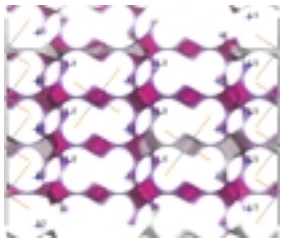

Li_8SnO_6 (R-3,015104)

Fig. 1. Examples of isosurfaces of constant *E(Li)* as bond valence models of Li^+ ion migration pathways in ternary oxides. In each graph three isosurfaces corresponding to increasing site energies are superimposed (red, magenta, light blue). Li atoms are indicated as blue crosses and labelled. Other atom positions are indicated by line or stick models. Labels below each graph indicate the respective compound name, space group and ICSD database [14] code of the underlying structure data.

Pathways in high energy Lithium-ion battery cathode materials $LiFeSO_4F$ and $LiVPO_4F$

Framework materials based on phosphate and sulfate polyanion building blocks are increasingly regarded as favorable replacements for conventional oxide-based cathode materials in lithium-ion battery applications. The lithium insertion phases $LiFePO_4$ and $Li_3V_2(PO_4)_3$ were the first of such materials identified and characterized. Recently, a few groups have described the insertion properties of the lithium vanadium fluorophosphates, $LiVPO_4F$ and $Li_5V(PO_4)_2F_2$ [16-18]. $LiVPO_4F$ is iso-structural with the naturally occurring triclinic minerals tavorite ($LiFePO_4OH$) and amblygonite ($LiAlPO_4F$). The $LiVPO_4F$ structure comprises a 3-D framework built up from single chains of 2 distinct corner-sharing $[VO_4F_2]$ octahedra cross-linked via $[PO_4]$

tetrahedra [16] wherein the oxygen atoms are shared between the two environments. The strong inductive effect of the PO_4^{3-} anion, combined with the presence of structural F^-, moderates the energetic of the transition-metal redox couple such that the reversible lithium insertion reactions for $Li_{1-x}VPO_4F$ occurs at the unusually high operating potential of ca. 4.2V versus Li. More recently, analogous fluoro-sulfates $LiMSO_4F$ (M=Fe, Co, Ni) have also been synthesized [19-21] and found to be isostructural to $LiMgSO_4F$ and hence to $LiVPO_4F$ (though a different setting of the unit cell is chosen in the original publication). As $LiMSO_4F$ (M = Fe, Co, Ni etc.), is unstable at the temperatures of most solid state reactions ($LiFeSO_4F$ decomposes for temperatures ≥ 350°C) [19], it became accessible only via ionothermal synthesis in EMI-TFSI. Cells with $LiFeSO_4F$ cathodes and Li anodes deliver 85% of the theoretical specific capacity of 151 mAh g^{-1} at C1 rate without carbon coating or nanostructuring. *ac* conductivity of $LiFeSO_4F$ was found to be mainly ionic with $E_A = 0.99 \pm 0.01$ eV and $\sigma(300K) \approx 10^{-10}$ S cm^{-1}. From projections of the framework structure. Recham *et al.* [19] originally suggested 3 tunnels with large cross sections (along [100], [010], and [101]) as pathways for a presumed 3D Li^+ migration.

Here we investigate the characteristics of Li^+ ion migration pathways in $LiVPO_4F$ and $LiFeSO_4F$ using the bond valence (BV) approach and molecular dynamics simulations. Based on a snapshot of the relaxed MD simulated supercell at 300 K an average crystal structure model is constructed by projecting the positions of all atoms back into a single unit cell. The resulting structure model (Fig. 2-3) closely resembles the published preliminary XRD data. Besides a minor rotation of SO_4^{2-} the main difference is in the Li^+ distribution, which is characterized by a pronounced disorder along channels extending in the [111] direction with two weak Li density maxima. The averaging of Li positions around the occupancy maxima yields the two Li positions: Li(1) at 0.145, 0.571 0.633 with an occupancy $n = 0.6$; and Li(2) at 0.450, 0.854, 0.854 with $n = 0.4$. The two partially occupied sites form Li(2)-Li(1)-Li(1)-Li(2) channels || [111] with distances ranging from 1.92–2.12 Å favorable for Li^+ transport, while migration in any other direction – especially along the earlier proposed tunnels–requires hop distances ≥3.69 Å (Fig. 3).

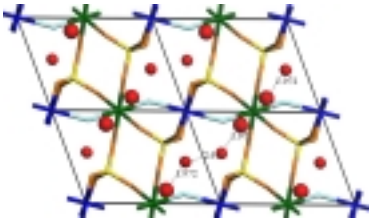

Fig. 2. Model of $LiFeSO_4F$ from MD simulations projected on *ac* plane (Fe(1) green, Fe(2) blue; S yellow; F light blue, O orange, Li red (occupancy 0.6 for Li(1) = large spheres, 0.4 for Li(2) = small spheres).

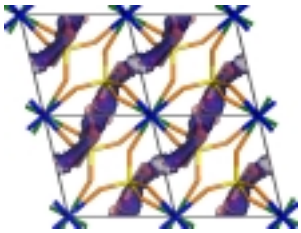

Fig. 3. Comparison of isosurface of constant Li density (dark) from MD trajectory (T = 600K) and BV pathway model (light) in a projection of the $LiFeSO_4F$ structure on the *ab* plane.

Static BV models for the Rietveld-refined and our MD simulated structure models [13] accordingly suggest zig-zag shaped 1D paths || [111] involving both Li sites as pathways of lowest migration energy barrier (≈ 0.22 eV), while a migration energy of ca. 0.97eV would be required to connect the channels in the [010] direction and an only slightly higher activation energy of 1.1eV leads to a 3D network of Li^+ migration pathways. Since low energy Li^+ pathways || [111] connect partially occupied Li sites, a defect formation should not be required for migration along these channels. The experimental $E_A = 0.99$ eV is much higher than the one predicted for migration along [111] channels, but closely resembles the E_A for the formation of a 2D pathway network (paths along [111] and [010]).

MD simulations of $LiVPO_4F$ have been conducted with GULP [22] using the Morse-type force field and a preliminary version of our *softBV* parameter set. Te starting unit cell was derived from crystallographic data for $LiAlPO_4F$ [23]. Simulations were based on a 3a×3b×3c supercell of the conventional setting. Note that the [111] diection in $LiFeSO_4F$ corresponds to the c-diection in $LiVPO_4F$. Geometry was optimized at T= 300 K. NVT MD simulations were performed at 300K to 1000K in intervals of 100K. At each temperature structures are equilibrated, followed by 2 ns production runs in 2 fs time steps. The diffusion co-efficients obtained from the slopes of the mean square displacement-vs.-time curves of simulations for T ≥ 600 K for individual directions indicate that

the mobility of Li+ is somewhat higher along the z-axis, while the activation is nearly the same (ca.0.5 eV) along all axes (Fig. 4).

BV models of the Li+ ion migration pathways in $LiVPO_4F$ suggest that the continuous pathway of lowest activation energy corresponds to a zig-zag shaped 1-D pathways along the z-axis (Fig. 5a-d).

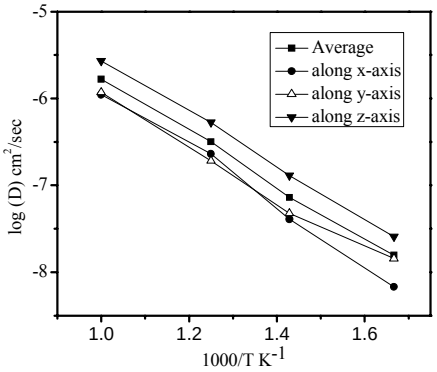

Fig. 4. Arrhenius plot of simulated diffusion coefficient for Li^+ ion along different Cartesian axes of the model system (with *z* || to the c axis).

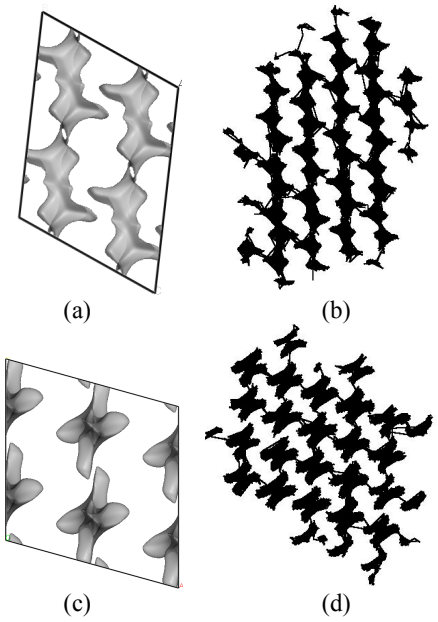

Fig. 5. BV models of Li^+ ion migration pathways in $LiVPO_4F$ displayed as isosurfaces of constant Li site energy *E(Li)* projected (a) on the xz-plane, (c) on the xy plane; compared to traces of Li motion of MD simulations in $LiVPO_4F$ supercells in matching orientations (b,d).

MD simulations of $LiFePO_4$ and surface modified $LiFePO_4$ with the BV-based force-field

MD simulations have been conducted with GULP [22] using the Morse-type force field discussed above for models of bulk $Li_{0.99}FePO_4$ (with a single built-in $Li'_{Fe}/Fe^{\bullet}_{Li}$ antisite defect per 96 formula units), glassy $[(Li_2O)_{2/3}\ (P_2O_5)_{1/3}]_{411}$ and for a 4367 atoms 3D-periodic interface structure $[LiFePO_4]_{320}$- $[(Li_2O)_{2/3}\ (P_2O_5)_{1/3}]_{491}$ for 300K ≤ T v< 1000 K. Bulk and $LiFePO_4$: $Li_4P_2O_7$ heterostructure ensembles are equilibrated in NPT simulations over 600ps. The relaxed volume is then fixed and equilibration continued for 150ps at each temperature followed by 600 ps (for T=600-1000K), 1 ns (for T=500K), or 3ns (for T = 400-300K) production runs in 1.5 fs steps [11,13]. When constructing the interface model based on relaxed structure models of $LiFePO_4$ and glassy $Li_4P_2O_7$, the (010) surface of $LiFePO_4$ ⊥ to the [010] Li^+ migration channels is chosen, since it is both the most relevant surface for Li^+ transport and the most prominent face of $LiFePO_4$ nanoparticles. The extra charge in non-stoichiometric $Li_{0.99}FePO_4$ is distributed over all Fe cations to emulate a charge transfer on a time scale faster than that of ionic transport. Lattice constants and average linear thermal expansion coefficients (for $LiFePO_4$ simulated: 1.8×10^{-5} K^{-1}; experimental: 1.9×10^{-5} K^{-1}, Fig. 6) match literature experiments closely. Simulations for bulk Li_xFePO_4 (x = 95/96) yield diffusion coefficients, *D*(*Li*)||b, (Fig. 8) that are consistent with values of *D(Li)*||b derived from the experimental conductivity data by Amin *et al*. [24], but considerably higher than values reported by Li *et al*. [25]. The simulated E_A = 0.57eV for bulk $Li_{.99}$FePO4 is consistent with findings of various experimental and theoretical studies. A BV pathway analysis for both time-averaged and snapshot-type structure models of fully ordered $LiFePO_4$ harmonizes with ab initio studies in yielding zig-zag shaped one-dimensional Li^+ pathways ||b. The apparent contradiction to some of the experimental conductivity data implying a 2D nature of the Li^+ motion motivated our study to which extent local structure models that include likely defect scenarios affect the expected pathway dimensionality.

Due to the moderate energetic disadvantage of antisite defects (≈1.1 eV) [26] some antisite defects will even occur in equilibrated samples, but concentrations in real samples will be significantly higher due to the common sample non-equilibrium preparation routes and the vicinity of surfaces or interfaces. Antisite defects in $LiFePO_4$ have recently been visualized by scanning transmission electron microscopy [27]. As seen from BV pathway models (Fig. 7 a-d) As to be seen from the BV pathway models in Fig. 1 a, b for a model containing a single antisite defect pair, this defect affects the local Li^+ pathways is two ways: $Fe^{\bullet}_{Li}$ inside the pathway channel blocks the ion transport || *b*, while Li'_{Fe} opens up a new path ⊥ *b* between the Li channels.

This can also be seen in MD simulations for elevated temperatures (Fig. 7c,d). For sufficiently high antisite defect concentrations this may lead to long-range Li^+ transport perpendicular to the channels. Our Monte Carlo-type simulations suggest that the defect concentration required for a 2D percolating Li^+ pathway cluster can be reduced to about 2.2% if a significant energetic preference for the formation of antisite defect pairs close to existing defects is assumed in line with the experimental TEM findings.

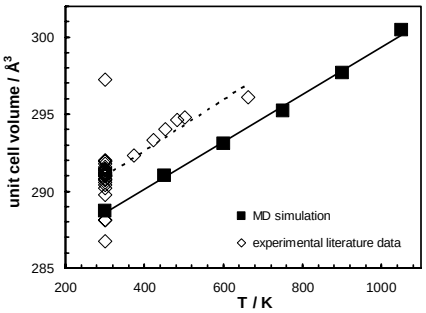

Fig. 6. Temperature dependent lattice constants of $LiFePO_4$ from MD simulations and exp. literature data.

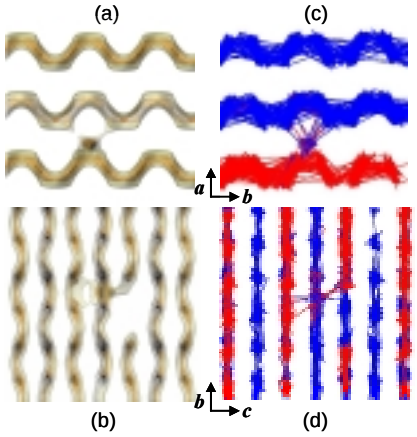

Fig. 7. (a,b) Projections of Li^+ pathway models in $Li_{.99}FePO_4$ with one antisite defect. The 3 super-imposed isosurfaces represent constant Li^+ site energy characteristic of equilibrium sites (black), migration channels || b (brown) and migration via antisite defects (beige). The BV based energy landscape approach yields the low-energy pathways even though at this temperature no transport ⊥b is observed during the simulated period of 1.5 ns. For comparison graphs (c,d) display Li^+ trajectories from MD simulations for T=1000K (1.5 ns). Atoms initially located in 1 b-c layer are marked in red.

Extraordinarily high (dis)charging rates were recently observed for cathodes with the nominal composition $LiFe_{0.9}P_{0.95}O_{4-\delta}$ [28]. Electron microscopy showed that the ca. 50 nm thin nanocrystals are phase segregated into Li_xFePO_4 and a surface layer of glassy $Li_4P_2O_7$ (or a similar composition) [28-30]. The phase segregation might also involve iron phosphides and/or Fe^{3+} in the glass, which would raise the electronic conductivity. Our MD simulations show that $D(Li)_{||b}$ in the $LiFePO_4$ layer is enhanced by ca. 3 orders of magnitude for typical working temperatures (Fig. 8). $D(Li)_{||b}$ in delithiated heterostructures is similar to the value for $x \approx 1$, while the anisotropy is less pronounced. Due to the reduced activation energy (= migration energy = 0.31eV for 300K ≤ T ≤ 700K), the conductivity enhancement practically vanishes for T > 700K, where E_A approaches the bulk value. Li^+ ions are significantly enriched on the Li_xFePO_4-side of the interface and depleted on the $Li_4P_2O_7$ glass side (Fig. 9). The overall Li^+ concentration in the Li_xFePO_4 layer increases by 4-7 % ("x=1") or 17-37% ("x=0.06") significant violation of local electroneutrality within each phase.

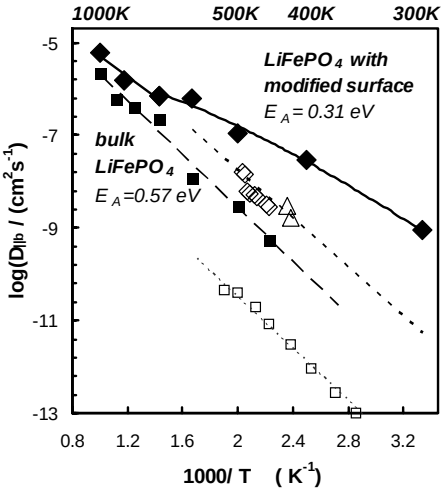

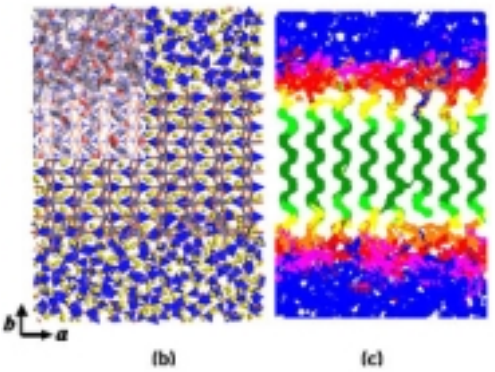

Fig. 8. (a) Comparison of simulation results for the Li^+ diffusion constant along the channel direction in $LiFePO_4$ from this work (■: bulk $LiFePO_4$; ♦: surface-modified $LiFePO_4$) with literature data (open symbols, experimental data: ◊,Δ [6], □ [24]). (b) Snapshot of MD simulations of $LiFePO_4$: $Li_4P_2O_7$ glass heterolayer for T=700K (Li: yellow, PO_4: blue tetrahedra, Fe grey). Inset: superposition of the Li BV pathways in 1/8 of this structure snapshot. Vacant parts of the pathway are marked in red, while pathway regions close to a Li^+ are marked in blue. (c) Trace of Li^+ motion in $LiFePO_4$: $Li_4P_2O_7$ heterolayer for 500 snapshots over 600ps (T=700K).

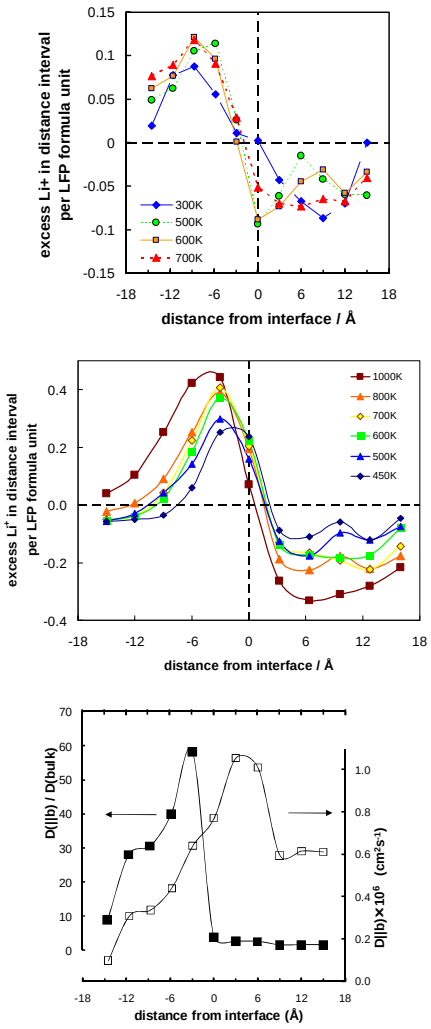

Fig. 9. Li^+ redistribution at the Li_xFePO_4:$Li_4P_2O_7$ interface displayed as % excess Li^+ in ca. 3Å thick slices vs. distance of the slice from the interface (l.h.s.: x=1; centre: x = 0.06). Li^+ ions are enriched in the Li_xFePO_4 phase (negative distances), depleted in the $Li_4P_2O_7$ glass. Each value represents an average over 100 - 250 MD time steps. R.h.s.: Variation of (■) relative Li^+ diffusion coefficient enhancement (compared to respective bulk values) and (□) absolute Li^+ diffusion coefficient $||b$ with the distance of the slice from the interface (T=600K, x=1).

The change in the extent of Li^+ redistribution with x implies a fast pseudo-capacitive energy storage component. Moreover, antisite formation near the interface boosts Li^+ mobility $\perp b$ and promotes a full utilization of the (dis)charging capacity (but slows down transport $\| b$). A layer-by-layer analysis of Li^+ displacements reveals that Li^+ mobility $||b$ is enhanced in the interface region (compared to bulk values) by a factor of 60 (T=600K) to ca. 3000 (T=300K) in harmony with the maximum of the volume fraction of low BV mismatch regions at the interface (Fig. 6). The relative enhancement is highest in Li_xFePO_4, while for T≥600K $D(Li)_{||b}$ is higher on the glass side of the interface. The anisotropy $D(Li)_{||b}$ / $D(Li)_{\perp b}$ is gradually reduced from practically infinite in $LiFePO_4$ to (trivially) one within the glass (partly via antisite defects, partly via Li^+ crossing the interface). Over ca. 1nm from the interface $D(Li)_{\perp b}$ in $LiFePO_4$ drops by a factor ≈90. As for "x = 0.06" most Li^+ reside close to the interface, the overall anisotropy of $D(Li)$ becomes a function of x. Despite their increased concentration in subsurface $LiFePO_4$, Li^+ ions find a sufficient number of accessible unoccupied target sites for migration. This is demonstrated in Fig. 10 by the variation of the volume fraction accessible for Li^+ migration.

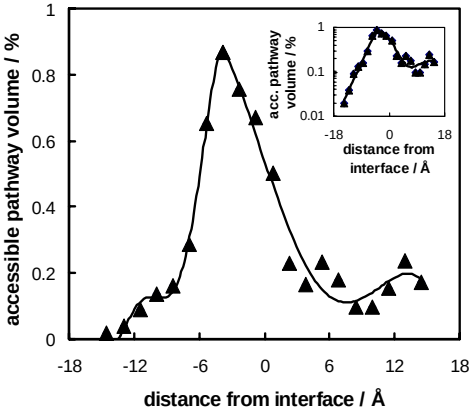

Fig. 10. Variation of accessible pathway volume fraction (regions of low Li^+ site energy < 0.6 eV that are not blocked by nearby Li^+ ; distance to Li > 2.5 Å) within 3 Å slices of MD-simulated $LiFePO_4$:$Li_4P_2O_7$ *vs.* distance from interface (averaged over 5 MD time frames at 600 ps intervals, T=300K). Solid lines: polynomial fits. The logarithmic plot of the same data (inset) highlights the exponential increase of the accessible pathway volume fraction within $LiFePO_4$ when approaching the interface.

CONCLUSIONS

The bond valence approach has been reworked into an effective local force-field that can be used both to analyse ion transport pathways and fo Molecular dynamics simulations. $LiFeSO_4F$ and $LiVPO_4F$ are thereby found to be quasi-one dimensional Li^+ ionic conductors (along channels that for $LiFeSO_4F$ extend along [111]). The experimental activation energy and power performance is however controlled by the moderate activation energy for transport perpendicular to the low energy pathways, which (as typical for 1D pathway channels) will in most cases be blocked by defects. The blocking could be overcome by nanostructuring.

The approach can also help to understand the effect of homogeneous and heterogeneous defects on the ionic of $LiFePO_4$, highlighting that the

dimensionality of ionic motion will depend on the concentration and spatial distribution of antisite defects. Surface modification of Li_xFePO_4 nanocrystals by glassy $Li_4P_2O_7$ causes a significant Li^+ redistribution entailing an enhancement of Li^+ mobility and an thus an enhancement of room temperature Li^+ ion diffusion by about 3 orders of magnitude along the channels. This and the drastically enhanced mobility perpendicular to the Li channel direction will facilitate a fast (dis)charging of Li batteries based on surface-modified $LiFePO_4$ electrodes. The pronounced change in the extent of the Li^+ redistribution from the phosphate glass layer into subsurface Li_xFePO_4 with x constitutes an ultrafast pseudocapacitive storage component.

ACKNOWLEDGMENT

Financial support in the frame of the Singapore Ministry of Education Grant MOE2009-T2-1-065 is gratefully acknowledged.

REFERENCES

1. S. Adams, J. Power Sources **159** (2006) 200.
2. J. Swenson and S. Adams, Phys. Rev. B **63** (2000) 054201.
3. C. Müller E. Zienicke, S. Adams, J. Habasaki and P. Maass, Phys. Rev. B **75** (2007) 014203.
4. S. Adams and R. Prasada Rao, Phys. Chem. **11** (2009) 3210.
5. I.D. Brown, Chem. Rev. **109** (2009) 6858.
6. S. Adams and E. S. Tan, Solid State Ionics **179** (2008) 33.
7. S. Adams, Solid State Ionics **177** (2006) 1625.
8. S. Adams, Acta Crystallogr. B **57** (2001) 278.
9. S. Adams, SoftBV ver. 0.96, http:// www.softBV.net. (2004).
10. I.D. Brown, Acta Crystallogr. B **48** (1992) 553.
11. S. Adams, Journal of Solid State Electrochemistry **14** (2010) 1787.
12. R. Prasada Rao, T.D Tho and S. Adams, Solid State Ionics **181** (2010) 1.
13. S. Adams and R. Prasada Rao, Submitted to Solid State Ionics (2010).
14. ICSD Inorganic Crystal Structure Database, FIZ Karlsruhe.
15. N.A. Anurova**,** V.A. Blatov, G.D. Ilyushin, O.A. Blatova, A.K. Ivanov-Schitz and L.N. Dem'yanets, Solid State Ionics **179** (2008) 2248.
16. J. Barker, R.K. B. Gover, P. Burns, A. Bryan, M.Y. Saidi and J.L. Swoyer, J. Electrochem. Soc. **152** (2005) A1776.
17. J. Barker, M.Y. Saidi, R.K.B. Gover, P. Burns and A. Bryan, J. Power Sources **174** (2007) 927.
18. S.C. Yin, P. Subramanya Herle, A. Higgins, N.T. Taylor, Y. Makimura and L.F. Nazar, Chem. Mater. **18** (7) (2006) 1745.
19. N. Recham, J.N. Chotard, L. Dupont, C. Delacourt, W. Walker, M. Armand and J.M. Tarascon, Nat. Mater. **9** (2010) 68.
20. J.M. Tarascon, N. Recham, M. Armand, J.N. Chotard, P. Prabanda, W. Walker and L. DuPont, Chem. Mater. **22** (2010) 724.
21. P. Barpanda, N. Recham, J.N. Chotard, K. Djellab, W. Walker, M. Armand and J.M. Tarascon, J. Mater. Chem. **20** (2010) 1659.
22. J.D. Gale, J. Chem. Soc. Faraday Trans. **93** (1997) 629.
23. V.I. Simonov and N.V. Belov, Kristallografiya **3** (1958) 428.
24. R. Amin and J. Maier, Solid State Ionics **178** (2008) 1831; R. Amin, J. Maier, P. Balaya, D.P. Chen and C.T. Lin, Solid State Ionics **179** (2008) 1683.
25. J. Li, W. Yao, S. Martin and D. Vaknin, Solid State Ionics **179** (2008) 2016.
26. C.A.J. Fisher, V.M.H. Prieto and MS. Islam, Chem. Mater. **20** (2008) 5907.
27. S.Y. Chung, S.Y. Choi, T. Yamamoto and Y. Ikuhara, Phys. Rev. Lett. **100** (2008) 125502.
28. B. Kang and G. Ceder, Nature **458** (2009) 190.
29. G. Ceder and B. Kang, J. Power Sources **194** (2009) 1024.
30. K. Zaghib, J.B. Goodenough, A. Mauger and C. Julien, J. Power Sources **194** (2009) 1021.